Supporting Information

Quantum Chemical Elucidation of the Luminescence Mechanism in Europium (III) co-doped UiO-66 Chemosensor Selective to Mercury (II)

Yoan Hidalgo-Rosa[a,b], Yoslainy Echevarria-Valdés[c], Mario Saavedra-Torres[d] Dayán Páez-Hernández[c,e], Eduardo Schott[f]* and Ximena Zarate[d]*

[a]Centro de Nanotecnología Aplicada, Facultad de Ciencias, Ingeniería y Tecnología, Universidad Mayor, Camino La Pirámide 5750, Huechuraba, Santiago, Chile. yoanhrj@gmail.com

[b]Escuela de Ingeniería del Medio Ambiente y Sustentabilidad, Facultad de Ciencias, Ingeniería y Tecnología, Universidad Mayor, Camino La Pirámide 5750, Huechuraba, 8580745 Santiago, Chile

[c]Doctorado en Fisicoquímica Molecular, Facultad de Ciencias Exactas, Universidad Andrés Bello, República 275, Santiago 8370146, Chile.

[d]Instituto de Ciencias Aplicadas, Facultad de Ingeniería, Universidad Autónoma de Chile, Av. Pedro de Valdivia 425, Santiago, Chile. ximena.zarate@uautonoma.cl

[e]Center of Applied Nanosciences (CANS), Universidad Andres Bello. Ave. República #275, 8370146 Santiago de Chile, Chile.

[f]Departamento de Química Inorgánica, Facultad de Química y de Farmacia, Centro de Energía UC, Centro de Investigación en Nanotecnología y Materiales Avanzados CIEN-UC, Pontificia Universidad Católica de Chile, Vicuña Mackenna 4860, Macul, 7820436 Santiago, Chile. maschotte@gmail.com; edschott@uc.cl

Corresponding Authors

Eduardo Schott. maschotte@gmail.com; edschott@uc.cl

Ximena Zarate. ximena.zarate@uautonoma.cl

Table of contents.

1. Computational Methods

1.1. Periodic models modelling of M^{n+}@UiO- 66(DPA)

UiO-66 native cells were employed to model Eu^{3+}@UiO-66(DPA) and Hg^{2+}@UiO-66(DPA), utilizing the crystal structure allocated on Cambridge Crystallographic Data Centre (CCDC), entry 1018045[1,2]. . The unit cell was reduced by symmetry to a primitive cell, corresponding with a rhombohedral shape. The coordination site for Eu^{3+} in UiO-66(DPA) was defined based on structural and spectroscopic evidence provide in the experimental reports.[3] XRD analysis confirms that UiO-66(DPA) retains the isostructural framework of UiO-66, with the DPA linker coordinating to Zr^{4+} via one carboxylate group while leaving the other carboxylic acid group and pyridine nitrogen atom free. XPS further corroborates that Eu^{3+} ions successfully coordinate to these free functional groups without disrupting the MOF's crystalline structure. Furthermore, considering that the proposed mechanism is based on the substitution of Eu^{3+} by Hg^{2+} at this site (*i.e.*, DPA linker), which induced the change in the Eu^{3+}@UiOUiO-66(DPA) optical properties. [3] This coordination environment was used as the basis for simulating the incorporation of Hg^{2+} into UiO-66(DPA), as it reflects the experimentally supported binding behavior of DPA towards Hg^{2+} ions.

All calculations were modeled through a linear combination of atomic orbitals (LCAO) periodic approximations [4], using R^2SCAN *meta*-generalized gradient approximation functional (MGGA)[5] in combination with PseudoDojo family of basis set pseudopotentials [6]. The Fermi-Dirac smearing occupancy method was used [7, 8] and 3x3x3 Monkhorst-Pack k-point scheme[9] was used to sample the first Brillouin zone considering a density cutoff of 140 hartrees (280 ryd). Moreover, a 5x5x5 Monkhorst-Pack k-point scheme was employed to obtain accurate band-gap data and Projected Density of State (PDOS). QuantumATK 2022.12 [8] was used for all ab initio calculations; Finally figures have been represented through VESTA software [10] and VMD 1.9.3 [11].

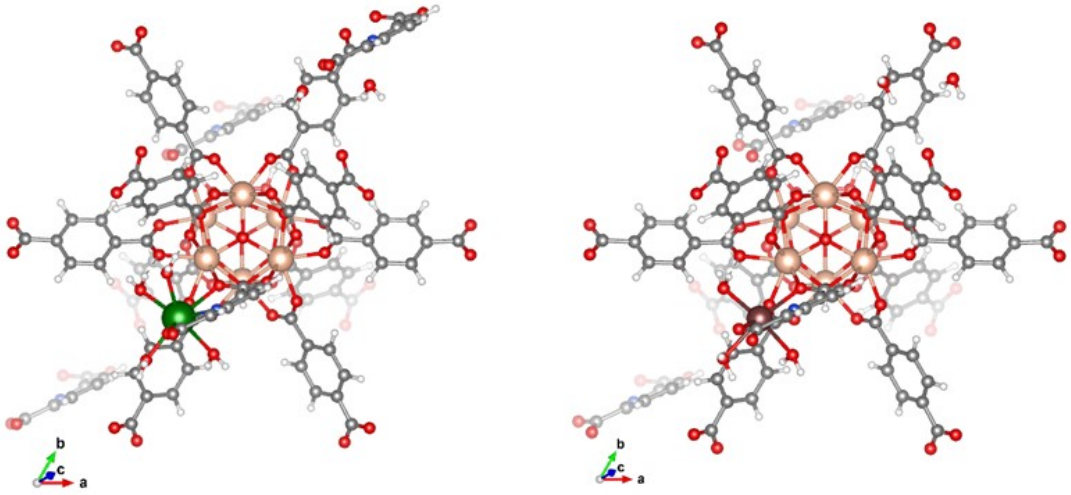

Figure S1 Expanded representation of **(a)** Eu^{3+}@UiO- 66(DPA) and **(b)** Hg^{2+}@UiO- 66(DPA)

Finally, to investigate the geometric properties and the underlying system, a supercell was constructed based on the previously established rhombohedral models of Eu and Hg. These models were combined into a 2x1x1 supercell with dimensions a = 29.50 Å, b = c = 14.75 Å, and angles α = β = γ = 60°. Each unit cell within the supercell contains a node and a ligand associated with each metal, Eu and Hg, respectively, see Figure S2. The atomic coordinates of the supercell were optimized using a 2x3x3 k-point grid, while adhering to the previously specified methodological parameters.

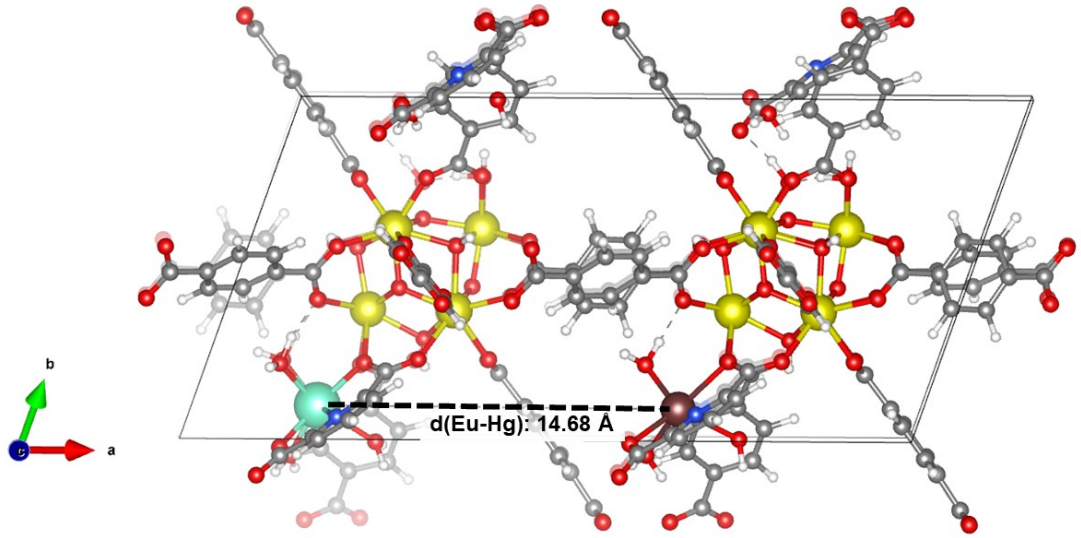

Figure S2. Supercell representation of **(a)** Hg^{2+}–Eu^{3+}@UiO- 66(DPA) . Interatomic distance Eu-Hg is representen in angstrom (Å).

Quantum mechanical calculations of Ln^{3+}-based systems are quite complex due to the unique electronic configurations of the Ln^{3+} ions $[Xe]4f^n$ and their strong electron correlation effects [12,13]. They have partially filled 4*f* orbitals, which can accommodate up to 14 electrons $[Xe]4f^n$ (n = 0-14). This results in a wide array of possible electronic configurations and energy levels with well-defined energies due to shielding effect of the 4f electrons by the outer 5s and 5p electrons [14]. Nonetheless, it is well-known that low absorption coefficients of lanthanide ions 4*f*–4*f* transitions due to the Laporte forbidden nature of the *f-f* transitions. Hence, the excitation energy is usually provided by the organic ligands, which strongly absorb light [15]. The organic ligand absorbs light and transfers energy to the lanthanide ions, which emits light at a different wavelength. This process, known as sensitization of luminescence or antenna effect, was discovered by Weissman in the year of 1942 [16].

1.2. Cluster model (finite fragment of the Eu^{3+}@UiO- 66(DPA) and Hg^{2+}@UiO- 66(DPA)).

This study aims to theoretically explore the electronic structure and luminescent properties of UiO-66 MOFs doped with Eu^{3+} ions to understand the luminescent sensing process toward Hg^{2+} ions. Due to the large size of the MOF, conducting comprehensive theoretical study using quantum mechanical methodologies is challenging. However, by employing a truncated cluster models, a small segment of the material can be effectively studied using advanced theoretical methods [17, 18]. The electronic structure and properties of MOFs for different applications such as catalysis, [19] chemical sensing,[20] gas storage and gas separation [21] are being studied using the cluster model approach. This approach is based on the fact that these materials have a unique electronic configuration that is characterized by highly localized electronic states [17]. The process to generate the cluster model involves as first step selecting a fragment to truncate from the optimized extended system of Eu^{3+}@UiO- 66(DPA) and Hg^{2+}@UiO-66(DPA) and conducting calculations to determine the sensitization, emission channels, and the sensing mechanism of Eu^{3+}@UiO- 66(DPA).

The proposed structural model for the Eu^{3+}@UiO-66(DPA) systems is composed by the fragment $[Zr_6O_4(OH)_4(BDC)_3(DPA\text{-}Eu^{3+})(HCOO)_8]$, extracted from the optimized structure of the material via periodic-DFT . This report presents a cluster model that includes a single node $[Zr_6O_4(OH)_4]^{12-}$, three complete BDC linkers, one DPA linker, eight truncated linkers using a formate ($HCOO^-$) group. The suggested structural model for the Hg^{2+}@UiO-66(DPA) systems includes the fragment $[Hg^{2+}@Zr_6O_4(OH)_4(BDC)_3(DPA)(HCOO)_8]$. A visual representation of this can be found in **Figure S3 (a)** and **(b).**

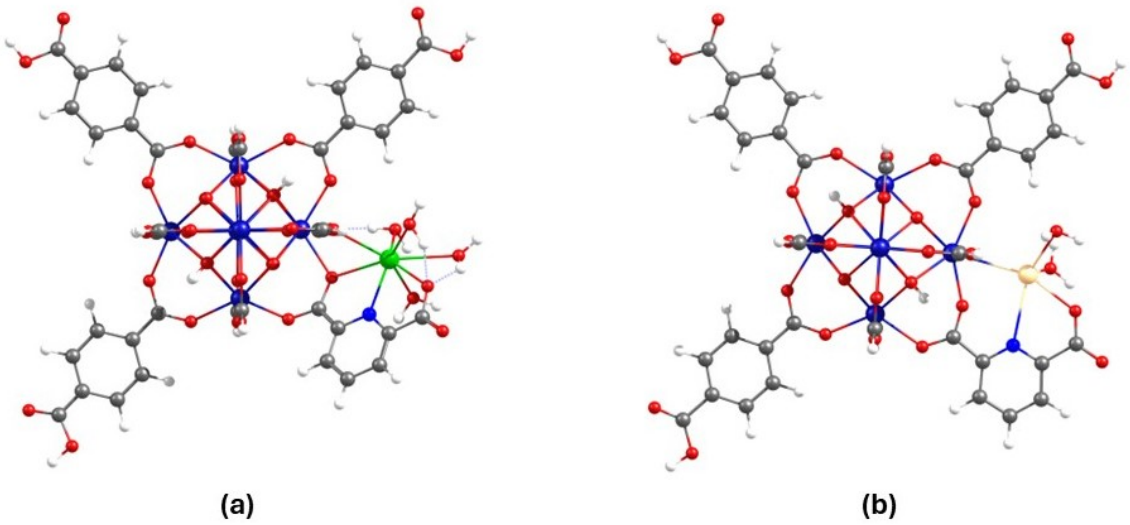

Figure S3. Cluster model (finite fragment truncated of the extended systems). (a) cluster model of the Eu^{3+}@UiO- 66(DPA) and (b) cluster model of the Hg^{2+}@UiO- 66(DPA).

1.3 Density Functional Theory (DFT) method

The finite fragment structures (cluster model) cut from the optimized extended structure were used as data input for single point calculations with their frequency calculation. The calculations were done using Density Functional Theory (DFT) method and the ORCA 5.0 package [22, 23].

The basis set, triple-ζ valence with two sets of polarization functions, def2-TZVPP, [24] was used for the C, H, N and O atoms, with the generalized gradient approximation (GGA) Perdew-Burke-Ernzerhoff (PBE) exchange correlation functional[25]. Also, the RIJCOSX approximation was used to accelerate the SCF calculation by the combination of the RIJ method for the Coulomb term with the "chain of spheres" COSX approximation and their respective auxiliary basis set for computation of two-electron integrals, [26, 27].

All optical properties were calculated using time-dependent DFT (TD-DFT) techniques with a revised version of ωB97M-V, including the D3BJ correction by Najibi [28, 29]. The inclusion of scalar relativistic effects was achieved using of the Douglas-Kroll-Hess Hamiltonian [30]. The relativistically re-contracted SARC2-DKH-QZV basis set was utilized to treat the europium atoms [31]. Meanwhile, the Stuttgart–Dresden effective core potential (ECP) was used for the zirconium and mercury atoms [32]. The SD(28, MWB) and SD(60, MWB) ECPs were considered for the zirconium and mercury, respectively. The ECP replaced 28 and 60 core electrons for zirconium and mercury atoms, respectively, while the def2-TZVPP basis set was used to treat the remaining electrons [24, 32].

For a more detailed analysis of the probable activation or deactivation pathway of the luminescence in Hg^{2+}@UiO-66(DPA) system the kinetic parameters associated this process were performed [33].

Specifically, the radiative rate (k_{rad}) and radiative lifetime (τrad) of the emission were determined using the emission energy ($\Delta E_{i,j}$) and the transition dipole moment ($\mu_{i,j}$) (Equation (1))[34,35].

$$k_{rd}(i \rightarrow f) = \frac{1}{\tau_{rd}} = \frac{4e^2}{3c^3\hbar^4}\left(\Delta E_{i,j}\right)^3\left(\mu_{i,j}\right)^2$$

To deepen our understanding of the sensitization pathways in Eu^{3+}@UiO-66(DPA), we investigated the excited-state dynamics of the antenna linker. This analysis was conducted using the fragmentation scheme proposed by M.J. Beltrán-Leiva et al. for lanthanide-based organometallic complexes.[36] The methodology involved geometry optimizations and frequency calculations for the ground state and the first excited states (singlet and triplet) of the systems.[36 37] Utilizing the ORCA ESD module from the ORCA 5.0.3 software package, [23] we determined the rates for intersystem crossing (k_{ISC}), phosphorescence (k_P), and fluorescence (k_F)[38]. The energy transfer rates were determined using time-dependent density functional theory (TD-DFT) calculations in conjunction with the LUMPAC software package,[39] (https://lumpac.pro.br/).

1.4 Multiconfigurational *ab initio* methods

To explore the most probable sensitization and energy-transfer pathways in lanthanide-based systems, it is essential to accurately describe the electronic states involved in these processes, including both the antenna ligand and the lanthanide ion[40 41]. However, semiempirical or DFT-based methods often leads to erroneous predictions of electronic states, particularly the triplet states of the antenna.[13] Furthermore, the theoretical treatment of lanthanide ions such as Eu^{3+} requires the use of multiconfigurational ab initio methods due to the complex electronic configuration of the 4f shell, which features a large number of closely spaced-in-energy 4f states shielded by the outer 5s and 5p shells[42]. In this work, the sensitization and emission channels of Eu^{3+}@UiO-66(DPA) systems were investigated using the Complete Active Space Self-Consistent Field (CASSCF) method[43 44],employing the fragmentation scheme proposed by María J. Beltrán-Leiva et al[40].

This method has demonstrated effective results for lanthanide (Ln) complexes and Ln-based MOFs [13, 42, 41]. In this approach the antenna is separated as a fragment preserving its geometry within the complex. Both fragments *i.e.,* the antenna fragment and lanthanide fragment are treated at the same level of theory, via the complete active space (CASSCF) approach [44]. For the proper application of this method, it's crucial to check that the absorption localized on the antenna ligand and the emission is originated from the lanthanide and ensures that the electronic transitions contributing to the sensitization process remain intact despite fragmentation [40]. In the first step the wave functions representing the ground and excited states of all fragments were obtained using the CASSCF method

[40, 41]. These fragments include the Eu-fragment and ligands fragments, (*i.e.,* BDC fragments and DPA fragments). In the second step, dynamic correlation effects were accounted for by applying the second-order N-electron Valence State Perturbation Theory (NEVPT2) to refine the energies obtained from the CASSCF calculations. [45] Taking into account that the configuration 4f shell of Eu^{3+} is $4f^6$ the chosen active space consisted of 6 electron in the 7 f-type orbitals, CAS(6,7)SCF. This active space CAS(6,7)SCF comprised of 7 septuplets, 60 quintuplets, 21 triples, and 21 singlets [46].

The energy values of the S_0, S_1 and T_1 electronic states for the BDC fragment and DPA fragment were computed, considering 30 singlets and 30 triplets, using the same level of theory employed for de Eu^{3+} fragment. Thus, the active space for the linkers, (*i.e.*, BTTA, DPYT and BPDC), consists of 10 electrons in 10 molecular orbitals CAS(10,10)SCF, 2 of them with non-bonding nature and the 6 of π-type orbitals. The choice of active space was determined through an extensive evaluation of simulated electronic transitions implicated in the absorption spectra of this system.

2. Simulated absorption spectrum of Eu^{3+}@UiO-66(DPA)

Table S1. Nature and oscillator strengths (*f*) of the vertical electronic transitions calculated for Eu^{3+}@UiO-66(DPA)

System	band	λ_{Exp}	λ_{Theo}	*f*	Assignment
Eu^{3+}@UiO-66(DPA)	B	305	278	0.175	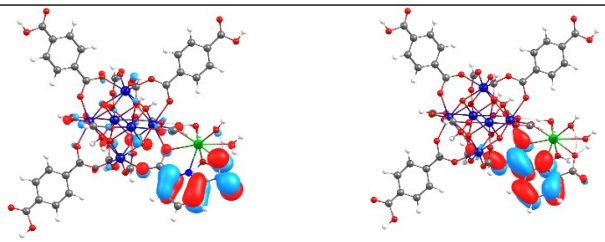 π(DPA)→ π*(DPA)
	A		272	0.970	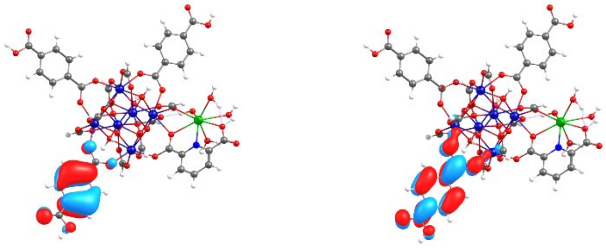 π(BDC)→ π*(BDC)

Note: λ_{Theo} is a computed wavelength value in nm, λ_{Exp} is an experimental value reported[3] and *f* is the oscillator strength.

3. Active orbitals and occupation numbers obtained for antenna fragment at CASSCF(10,10)/NEVPT2 level of theory

3.1 Active orbitals and occupation numbers obtained for antenna $[BDC]^{1-}$

Table S2. Active orbitals and occupation numbers obtained for antenna fragment $[BDC]^{1-}$ at CAS (10,10) SCF/NEVPT2 level of theory

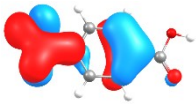	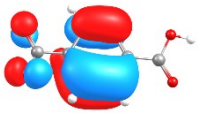	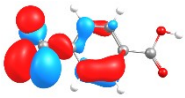		
π_1(1.80)	**π_2(1.64)**	**n_1(1.65)**	**π_3(1.63)**	**π_4(1.61)**
	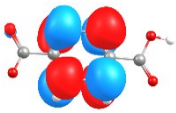	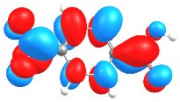	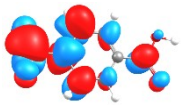	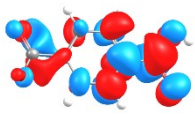
π_5(0.85)	**π_6(0.46)**	**π_7(0.22)**	**π_8(0.07)**	**π_2(0.02)**

S_0 80% $|\pi_1^2\pi_2^2\, n_1^2\, \pi_3^2\pi_4^2|$

S_1 50% $|\pi_1^2\pi_2^2\, n_1^2\, \pi_3^2\pi_4^1\pi_5^1|$ **($\pi\rightarrow\pi^*$)** **38%** $|\pi_1^2\pi_2^2\, n_1^1\, \pi_3^2\pi_4^2\, \pi_5^1|$ **($n\rightarrow\pi^*$)**

S_2 43% $|\pi_1^2\pi_2^2\, n_1^2\, \pi_3^1\pi_4^2\, \pi_5^1|$ **($n\rightarrow\pi^*$)** **30%** $|\pi_1^2\pi_2^2\, n_1^2\, \pi_3^2\pi_4^1\pi_6^1|$ **($\pi\rightarrow\pi^*$)**

T_1 78% $|\pi_1^2\pi_2^2\, n_1^2\, \pi_3^2\pi_4^1\pi_5^1|$ **($\pi\rightarrow\pi^*$)**

3.2 Active orbitals and occupation numbers obtained for antenna $[DPA]^{2-}$

Table S3. Active orbitals and occupation numbers obtained for antenna fragment $[DPA]^{2-}$ at CAS (10,10) SCF/NEVPT2 level of theory

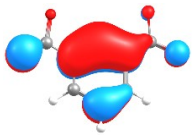	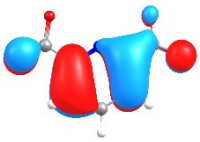	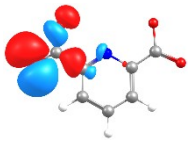	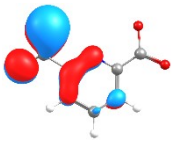	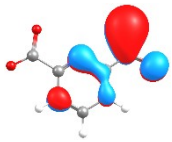
π_1(1.80)	**π_2(1.77)**	**n_1(1.75)**	**π_3(1.65)**	**π_4(1.46)**
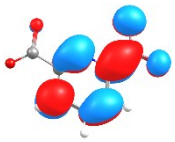	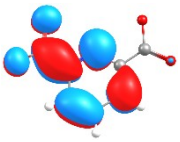		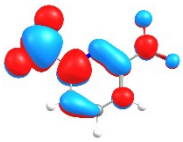	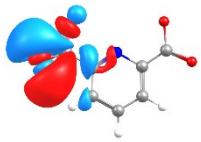
π_5(0.79)	**π_6(0.55)**	**π_7(0.14)**	**π_8(0.08)**	**n_2(0.02)**

S_0 80% $|\pi_1^2\pi_2^2\, n_1^2\, \pi_3^2\pi_4^2|$

S_1 50% $|\pi_1^2\pi_2^2\, n_1^2\, \pi_3^2\pi_4^1\pi_5^1|$ **(π→π*)** **20%** $|\pi_1^2\pi_2^2\, n_1^2\, \pi_3^2\pi_4^1\pi_7^1|$ **(π→π*)**

S_2 43% $|\pi_1^2\pi_2^2\, n_1^2\, \pi_3^1\pi_4^2\pi_5^1|$ **(π→π*)** **20%** $|\pi_1^2\pi_2^2\, n_1^2\, \pi_3^2\pi_4^1\pi_6^1|$ **(π→π*)**

T_1 78% $|\pi_1^2\pi_2^2\, n_1^2\, \pi_3^2\pi_4^1\pi_5^1|$ **(π→π*)**

4. Reference

1. S. Øien, D. Wragg, H. Reinsch, S. Svelle, S. Bordiga, C. Lamberti and K. P. Lillerud, *Cryst. Growth Des.*, 2014, **14**, 5370–5372.
2. S. Gražulis, A. Daškevič, A. Merkys, D. Chateigner, L. Lutterotti, M. Quirós, N. R. Serebryanaya, P. Moeck, R. T. Downs and A. Le Bail, *Nucleic Acids Res.*, 2012, **40**, 420–427.
3. Z. Xiaoxiong, Z. Wenjun, L. Cuiliu, Q. Xiaohong and Z. Chengyu, *Inorg. Chem.*, 2019, **58**, 3910–3915.
4. J. M. Soler, E. Artacho, J. D. Gale, A. García, J. Junquera, P. Ordejón and D. Sánchez-Portal, *J. Phys. Condens. Matter*, 2002, **14**, 2745–2779.
5. J. P. Perdew, K. Burke and M. Ernzerhof, *Phys. Rev. Lett.*, 1996, **77**, 3865–3868.
6. M. J. van Setten, M. Giantomassi, E. Bousquet, M. J. Verstraete, D. R. Hamann, X. Gonze and G. M. Rignanese, *Comput. Phys. Commun.*, 2018, **226**, 39–54.
7. N. D. Mermin, *Phys. Rev.*, 1965, **137**, 1–3.
8. S. Smidstrup, T. Markussen, P. Vancraeyveld, J. Wellendorff, J. Schneider, T. Gunst, B. Verstichel, D. Stradi, P. A. Khomyakov, U. G. Vej-Hansen, M. E. Lee, S. T. Chill, F. Rasmussen, G. Penazzi, F. Corsetti, A. Ojanperä, K. Jensen, M. L. N. Palsgaard, U. Martinez, A. Blom, M. Brandbyge and K. Stokbro, *J. Phys. Condens. Matter*, 2020, **32**, 015901.
9. J. D. Pack and H. J. Monkhorst, *Phys. Rev. B*, 1976, **13**, 5188–5192.
10. K. Momma and F. Izumi, *J. Appl. Crystallogr.*, 2011, **44**, 1272–1276.
11. K. Humphrey, W., Dalke, A. and Schulten, *J. Mol. Graph.*, 1996, **14**, 33-38.
12. B. Yan, *Inorg. Chem. Front.*, 2021, **8**, 201–233.
13. M. J. Beltrán-Leiva, D. Páez-Hernández and R. Arratia-Pérez, *Inorg. Chem.*, 2018, **57**, 5120–5132.
14. Y. Cui, B. Chen and G. Qian, *Elsevier*, 2014, DOI: 10.1016/j.ccr.2013.10.023.
15. M. Zeng, C. Zhan and J. Yao, *J. Mater. Chem. C*, 2019, **7**, 2751–2757.
16. S. I. Weissman, *J. Chem. Phys.*, 1942, **10**, 214–217.
17. J. L. Mancuso, A. M. Mroz, K. N. Le and C. H. Hendon, *Chem. Rev.*, 2020, **120**, 8641–8715.
18. R. Chakraborty, J. J. Talbot, H. Shen, Y. Yabuuchi, K. M. Carsch, H. Z. H. Jiang, H. Furukawa, J. R. Long and M. Head-Gordon, *Phys. Chem. Chem. Phys.*, 2024, **26**, 6490–6511.
19. X. P. Wu, L. Gagliardi and D. G. Truhlar, *J. Am. Chem. Soc.*, 2018, **140**, 7904–7912.
20. U. Mondal, K. Raksha, P. Mondal and P. Banerjee, *Chem. - An Asian J.*, 2024, **19**, e202400374.
21. M. U. C. Braga, G. H. Perin, L. H. de Oliveira and P. A. Arroyo, *Adsorption*, 2024, **30**, 519–535.

22. F. Neese, *Wiley Interdiscip. Rev. Comput. Mol. Sci.*, 2018, **8**, e1327.

23. F. Neese, *John Wiley and Sons Inc*, 2022, DOI: 10.1002/WCMS.1606.

24. F. Weigend and R. Ahlrichs, *Phys. Chem. Chem. Phys.*, 2005, **7**, 3297–3305.

25. J. P. Perdew, K. Burke and M. Ernzerhof, *Phys. Rev. Lett.*, 1996, **77**, 3865–3868.

26. F. Neese, F. Wennmohs, A. Hansen and U. Becker, *Chem. Phys.*, 2009, **356**, 98–109.

27. G. L. Stoychev, A. A. Auer and F. Neese, *J. Chem. Theory Comput.*, 2017, **13**, 554–562.

28. S. D. George, T. Petrenko and F. Neese, DOI:10.1021/jp803174m.

29. A. D. Becke, *J. Chem. Phys.*, 1993, **98**, 5648–5652.

30. B. A. Hess, *Phys. Rev. A*, 1986, **33**, 3742–3748.

31. J. D. Rolfes, F. Neese and D. A. Pantazis, *J. Comput. Chem.*, 2020, **41**, 1842–1849.

32. D. Andrae, U. Häußermann, M. Dolg, H. Stoll and H. Preuß, *Theor. Chim. Acta*, 1990, **77**, 123–141.

33. M. A. Treto-Suárez, Y. Hidalgo-Rosa, E. Schott, X. Zarate and D. Páez-Hernández, *Int. J. Quantum Chem.*, 2020, **120**, 26083.

34. E. A. Briggs and N. A. Besley, *J. Phys. Chem. A*, 2015, **119**, 2902–2907.

35. R. A. Marcus, *Angew. Chem., Int. Ed. Engl.* ., 1993, **32**, 1111−1121.

36. M. J. Beltrán-Leiva, E. Solis-Céspedes and D. Páez-Hernández, *Dalt. Trans.*, 2020, **49**, 7444–7450.

37. J. J. Santoyo-Flores and D. Páez-Hernández, *Int. J. Quantum Chem.*, 2022, **122**, e26880.

38. Y. Hidalgo-Rosa, K. Mena-Ulecia, M. A. Treto-Suárez, E. Schott, D. Páez-Hernández and X. Zarate, *J. Phys. Chem. A*, 2022, **126**, 7040–7050.

39. J. D. L. Dutra, T. D. Bispo and R. O. Freire, *J. Comput. Chem.*, 2014, **35**, 772–775.

40. M. J. Beltrán-Leiva, P. Cantero-López, C. Zúñiga, A. Bulhões-Figueira, D. Páez-Hernández and R. Arratia-Pérez, *Inorg. Chem.*, 2017, **56**, 9200–9208.

41. Y. Hidalgo-Rosa, M. A. Treto-Suárez, E. Schott, X. Zarate and D. Páez-Hernández, *J. Comput. Chem.*, 2020, **41**, 1956–1964.

42. Z. Abbas, S. Dasari, M. J. Beltrán-Leiva, P. Cantero-López, D. Páez-Hernández, R. Arratia-Pérez, R. J. Butcher and A. K. Patra, *New J. Chem.*, 2019, **43**, 15139–15152.

43. B. O. Malmqvist, P.-Á. & Roos, *Chem. Phys. Lett.*, 1989, **155**, 189–194.

44. B. O. Roos, P. R. Taylor and P. E. M. Sigbahn, *Chem. Phys.*, 1980, **48**, 157–173.

45. C. Angeli, R. Cimiraglia and J. P. Malrieu, *Chem. Phys. Lett.*, 2001, **350**, 297–305.

46. Z. Abbas, S. Dasari, M. J. Beltrán-Leiva, P. Cantero-López, D. Páez-Hernández, R. Arratia-Pérez, R. J. Butcher and A. K. Patra, *New J. Chem.*, 2019, **43**, 15139–15152.